EES Solar

PAPER

View Article Online
View Journal | View Issue

Cite this: *EES Sol.*, 2025, **1**, 620

Optimizing 2D passivation for enhancing performance of fully air-processed carbon electrode-based perovskite solar cells†

Kausar Ali Khawaja,[a] S. N. Vijayaraghavan,[b] Saivineeth Penukula,[c] Wenjun Xiang,[a] Nicolas Rolston,[c] Lin Li[a] and Feng Yan *[a]

Air-processed carbon-based perovskite solar cells (C-PSCs) offer scalable and cost-effective photovoltaic manufacturing but face efficiency loss compared to metal-contact perovskite solar cells. Surface passivation of three-dimensional (3D) perovskites with two-dimensional (2D) perovskite layers has emerged as a promising strategy to enhance device performance. However, the mechanisms by which 2D perovskites more effectively improve C-PSC efficiency and stability remain underexplored. This study investigates the efficacy of 2D/3D heterostructures using *n*-hexylammonium bromide (C_6Br), phenethylammonium iodide (PEAI), and *n*-octylammonium iodide (OAI) as surface passivators for C-PSCs. C-PSCs treated with C_6Br achieved a champion power conversion efficiency (PCE) of 21.0%. This enhancement is attributed to superior defect passivation, improved charge extraction, and suppressed non-radiative recombination. Transient ion-drift characterization demonstrates that C_6Br and OAI reduce ionic conductivity by 2–3 orders of magnitude, correlating with enhanced operational stability under continuous illumination. Our findings highlight the role of short-chain bromide cations (C_6Br) in optimizing halide-mediated defect healing and interfacial band alignment, positioning 2D-passivated C-PSCs as viable competitors to conventional metal-contact perovskite solar cells.

Received 22nd June 2025
Accepted 10th July 2025

DOI: 10.1039/d5el00099h

rsc.li/EESSolar

Broader context

Carbon-based perovskite solar cells (C-PSCs) are promising for low-cost, scalable photovoltaics due to their air-processability and metal-free architecture. However, their efficiency lags behind metal-contact PSCs, mainly due to interfacial defects and poor charge extraction. Two-dimensional (2D) perovskite passivation has shown promise, but its effects in C-PSC systems remain underexplored. This study demonstrates that short-chain 2D cations, particularly *n*-hexylammonium bromide (C_6Br), significantly enhance efficiency and operational stability by suppressing ionic conductivity and non-radiative recombination. These insights position 2D/3D-engineered C-PSCs as viable, efficient, and stable alternatives for sustainable photovoltaic applications.

Introduction

Perovskite solar cells (PSCs) have rapidly emerged as a leading photovoltaic technology, achieving remarkable power conversion efficiencies with certified power conversion efficiency above 27% due to their superior optoelectronic properties.[1] This progress has been driven by advances in stoichiometric tuning, crystallinity control, and interfacial engineering, all of which contribute to improved charge transport and reduced recombination losses.[2–5] Despite these achievements, the long-term operational stability of PSCs remains a major hurdle. Hybrid perovskite films are intrinsically sensitive to environmental stressors, such as moisture, heat, oxygen, and light, as well as internal degradation mechanisms, such as ion migration and phase segregation.[6–8] These issues hinder commercial viability and necessitate effective strategies to enhance stability. In parallel, carbon-based perovskite solar cells (C-PSCs), which utilize carbon electrodes instead of conventional metal contacts, *e.g.*, Au, Ag, and Cu, have attracted growing interest due to their low cost, chemical robustness, and compatibility with scalable, fully printable device architectures.[9–12] In particular, the hydrophobic carbon electrode can also protect the underlying perovskite layer against moisture attack, which provides enhanced stability. However, the efficiency of C-PSCs is significantly lower than that of metal electrode-based

[a]*Materials Science and Engineering Program, School for Engineering of Matter, Transport and Energy, Arizona State University, Tempe, AZ, 85287, USA. E-mail: fengyan@asu.edu*

[b]*Department of Metallurgical and Materials Engineering, The University of Alabama, Tuscaloosa, Alabama, 35487, USA*

[c]*School of Electrical, Computer, and Energy Engineering (ECEE), Arizona State University, Tempe, AZ, 85287, USA*

† Electronic supplementary information (ESI) available. See DOI: https://doi.org/10.1039/d5el00099h

PSCs, which limits the potential for large-scale manufacturing of carbon electrode-based perovskite solar modules.

Currently, one popular approach to improve the efficiency and stability of the perovskite solar cells is surface passivation *via* the formation of low-dimensional (2D) perovskite layers on the surface of the 3D perovskite layer. This is typically achieved by depositing bulky organic cations onto the 3D perovskite, forming a 2D/3D heterostructure by reaction with excess PbI_2. Such structures improve both chemical and structural stability by creating a hydrophobic, tightly packed surface 2D perovskite layer that resists environmental degradation.[13–17] In particular, these van der Waals interactions between large organic spacer cations in 2D perovskites further enhance their intrinsic stability, while also mitigating ion migration and surface defects.[18–21] When combined with 2D passivation strategies, C-PSCs may offer a compelling route toward stable and low-cost solar technologies.[22–26]

A variety of organic ammonium salts have been explored for 2D surface passivation. For example, phenethylammonium iodide (PEAI) and its derivatives have been widely used to form PEA_2PbI_4 capping layers on top of the 3D perovskite layer, which effectively passivates surface traps and often increases the open-circuit voltage (V_{oc}).[27–33] Similarly, alkylammonium cations such as *n*-octylammonium iodide (OAI) introduce hydrophobic long-chain structures that provide both defect passivation and environmental protection.[34–36] Recent studies have shown that tuning the chemical structure of 2D cations, such as through halogen substitution, can significantly influence interfacial dipoles and defect passivation, thereby enhancing device performance.[37,38] In addition, bromide-based cations, such as *n*-hexylammonium bromide ($CH_3(CH_2)_5NH_3Br$, C_6Br), have similarly shown promise in increasing V_{oc} through the formation of wider-bandgap 2D interfacial layers, *i.e.*, $(CH_3(CH_2)_5NH_3)_2PbI_4$.[28,39] While many 2D cations have been individually studied, comparative analyses under identical processing and testing conditions are limited. Such studies are essential for identifying optimal passivation agents and guiding rational device design to uncover the contribution of the 2D perovskite layer to C-PSC device performance.

In this work, we systematically test three widely used 2D cations applied as surface passivators to improve the C-PSC performance and elucidate the root cause for improved stability and efficiency, *i.e.*, *n*-hexylammonium bromide (C_6Br), phenethylammonium iodide (PEAI), and *n*-octylammonium iodide (OAI). These cations were chosen to represent a range of molecular features: C_6Br offers a short alkyl chain with a bromide anion, PEAI introduces an aromatic ring with iodide and is a widely used benchmark for performance enhancement, while OAI provides a longer alkyl chain known for its hydrophobicity and environmental resilience. Our results show that C_6Br yielded the highest power conversion efficiency (PCE) (~21%), followed by PEAI (19.7%) and OAI (17.6%). In terms of stability, both C_6Br and OAI retained 100% of their initial efficiency over 500 hours of continuous monitoring under a nitrogen atmosphere, highlighting the importance of both the cation structure and environmental control in achieving long-term PSC stability.

Experimental section

Materials

All materials were used directly without any purification, including PbI_2 (Sigma-Aldrich, 99.999%), FAI (GreatCell Solar, 99.99%), FABr (TCI, 98%), CsI (BeanTown Chemical, 99.9%), MACl (Sigma-Aldrich, 98%), SnO_2 precursor (Alfa Aesar, 15% in H_2O colloidal dispersion), *n*-octylammonium iodide (OAI, GreatCell Solar), *n*-hexylammonium bromide (C_6Br, GreatCell Solar, 99%), and phenethylammonium iodide (PEAI, Sigma-Aldrich, 98%). Spiro-OMeTAD, 4-*tert*-butylpyridine (*t*BP), bis(-trifluoromethane)sulfonimide lithium salt (Li-TFSI), and chlorobenzene were purchased from Sigma-Aldrich. Dimethylformamide (DMF), dimethyl sulfoxide (DMSO), isopropanol (IPA), acetonitrile, and diethyl ether (DEE) were obtained from Acros Organics.

Device fabrication

Indium-doped tin oxide (ITO) substrates were cleaned with detergent, deionized water (DIW), acetone, and IPA for 20 minutes sequentially, then dried by N_2 blowing followed by UV–ozone treatment for 20 minutes. The SnO_2 colloidal solution diluted by DIW was spin-coated at a speed of 3000 rpm for 30 s, followed by annealing at 150 °C for 30 minutes. Before the deposition of perovskite films, SnO_2 layers were treated with UV–ozone for 10 minutes. $Cs_{0.03}FA_{0.97}PbI_{2.96}Br_{0.04}$ perovskite precursor solution was prepared by dissolving 1.74 M PbI_2, 1.6 M FAI, 0.05 M FABr, 0.05 M CsI, and 0.5 M MACl in a mixed solvent of DMF and DMSO (8.5 : 1.5 v/v). The perovskite film deposition and annealing were performed under ambient conditions with a relative humidity (RH) of 30–40%. The perovskite solution was spin-coated on top of the SnO_2 layer using a two-step program: 1000 rpm for 10 seconds (low speed), followed by 5000 rpm for 30 seconds (high speed). 120 μL of chlorobenzene as an antisolvent was dropped 15 seconds before the end of the high-speed spin step. This timing is critical to promote uniform crystallization during the film formation process. The film was then annealed at 140 °C for 20 minutes. 2.5 mg of OAI, C_6Br, and PEAI were dissolved in 1 mL of IPA. 60 μL of the 2D solution was deposited on the perovskite film by spin-coating at 4000 rpm for 30 s. 72.3 mg of spiro-OMeTAD was dissolved in 1 mL of chlorobenzene, to which 28 mL of *t*BP and 17.5 mL of Li-TFSI (520 mg in 1 mL of acetonitrile) were added. 30 μL of spiro-OMETAD solution was then spin-coated at 4000 rpm for 30 s. The carbon electrode was applied as reported before.[40]

Materials and device characterization

Current density (*J*–*V*) was measured using a solar simulator (Newport, Oriel Class AAA 94063A, 1000 watt xenon light source) with a Keithley 2420 source meter under simulated AM 1.5G (100 mW cm^{-2}, calibrated with a standard Si solar cell) solar irradiation with a forward scan from −0.2 to 1.2 V and reverse scan from 1.2 V to 0.2 V, respectively. The active area was defined by a 0.08 cm^2 aperture. The EQE was obtained using an EnliTech QE measurement system. The PL and TRPL were

acquired using an Edinburgh Instruments FS5 spectrofluorometer. A PAIOS (all-in-one characterization equipment for photovoltaic devices and LEDs) was used to perform capacitance–voltage (*C–V*) measurements, electrochemical impedance spectroscopy (EIS), and dark *J–V* characterization. The scanning electron microscopy (SEM) images were obtained using an SEM/focused ion beam from Auriga (Zeiss) at an acceleration voltage of 5 kV. The X-ray diffraction (XRD) measurements were performed using a Rigaku SmartLab high-resolution X-ray diffractometer. The GIWAXS measurements were carried out using a Xenocs Xeuss (GI-)SAXS/WAXS/USAXS instrument with a GeniX3D Cu High Flux Very Long (HFVL) focus source as the X-ray source and an Eiger2 R 1M Dectris hybrid pixel silicon sensor as the detector.

Results and discussion

The perovskite solar cells employed an n–i–p architecture with glass/ITO/SnO_2/3D perovskite/2D passivation layer/spiro-OMeTAD/carbon (Fig. 1a), where bulky organic cations in the 2D capping layer, such as PEA^+, OA^+ and $CH_3(CH_2)_5NH_3^+$ interact with surface excess PbI_2 on top of the 3D perovskite to form a quasi-2D capping layer, effectively passivating surface defects associated with PbI_2. Grazing-incidence wide-angle X-ray scattering (GIWAXS) measurements provide direct evidence for forming 2D perovskite layers. The normalized in-plane GIWAXS intensity profiles (Fig. 1b) reveal distinct Ruddlesden–Popper (RP)-phase (001/002) reflections for all three passivated films (C_6Br, PEAI, and OAI), absent in the pristine specimen. The appearance of these RP-phase peaks is consistent with prior reports of 2D/3D heterostructured perovskites, where characteristic low-angle (001) reflections signify the formation of RP phases.[41] Notably, the OAI-passivated films exhibit a slight red shift in the RP-phase peak compared to C_6Br and PEAI (Fig. 1b), indicating an increased interlayer spacing within the quasi-2D perovskite structure. This expansion arises due to the longer alkyl chain of OAI, which widely separates the inorganic layers, forming a more relaxed 2D structure with longer-chain alkylammonium cations.[42,43]

A peak attributed to PbI_2 appears near $q \approx 0.85$ Å^{-1} in Fig. 1b, but its intensity is relatively weak and not clearly resolved due to overlap with the main perovskite background.

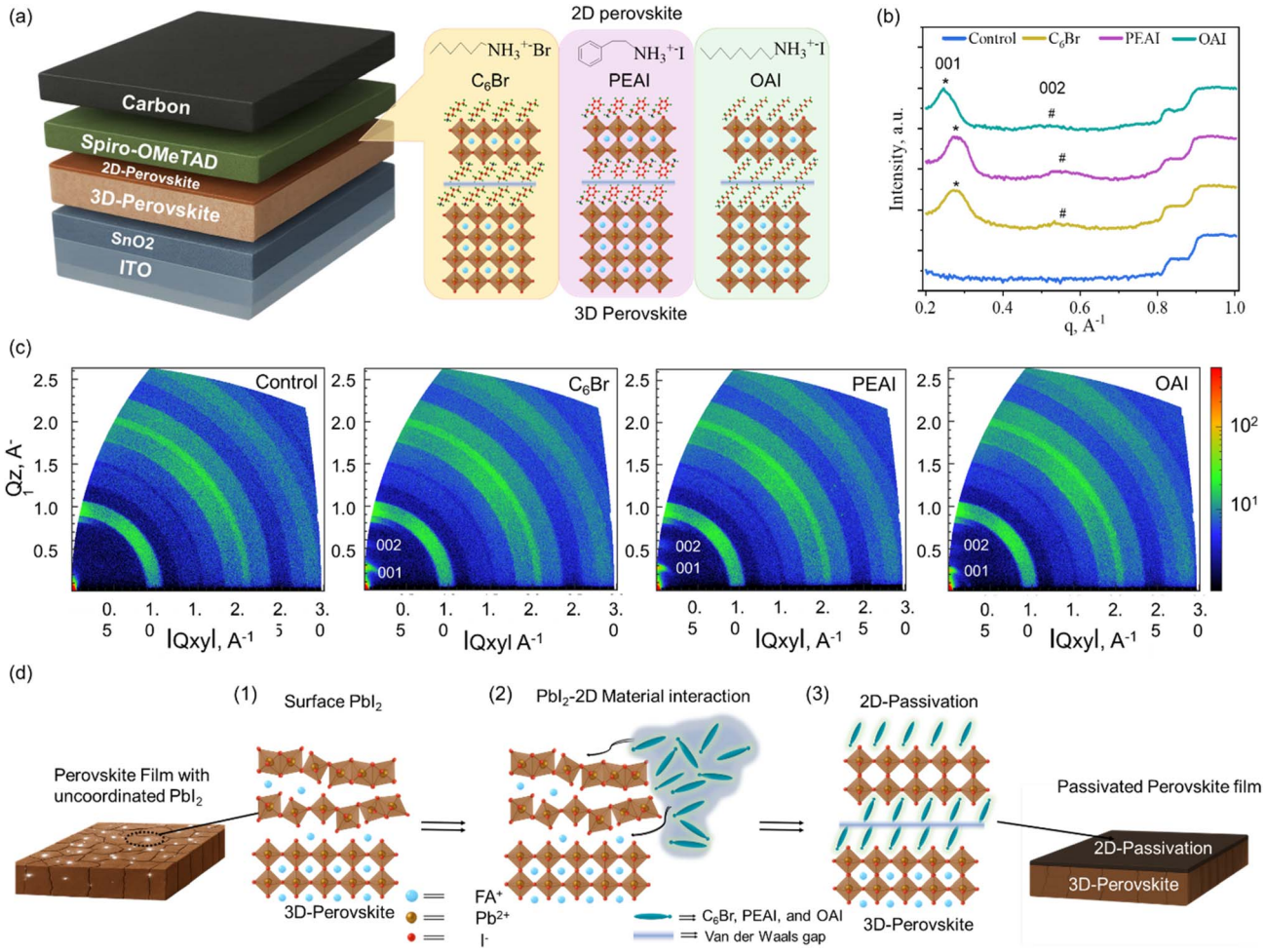

Fig. 1 (a) Schematic of the perovskite solar cell architecture with 2D passivation layers (C_6Br, PEAI, and OAI, respectively); (b) normalized in-plane GIWAXS intensity profiles; (c) 2D GIWAXS patterns showing 001/002 Ruddlesden–Popper-phase reflections indicating 2D perovskite formation; (d) illustration of the 2D passivation mechanism involving surface PbI_2 interaction, 2D layer formation, and passivated interface development.

This limitation stems from the larger sample area and beam footprint used during GIWAXS, which broaden features and reduce sensitivity to isolated crystalline impurities such as PbI_2. Therefore, we relied on XRD (Fig. 2b) to assess the PbI_2 content more accurately, while GIWAXS was primarily used to confirm the formation of quasi-2D RP phases. The detailed 2D passivation layer formation mechanism is schematically illustrated in Fig. 1d.

To further assess the impact of 2D passivation layers on surface chemistry and film quality, X-ray diffraction (XRD), UV-Vis absorption, and scanning electron microscopy (SEM) analyses were conducted. XRD spectra show clear evidence of reduced residual PbI_2 in passivated films compared to the control (Fig. 2a), where the main black phase 3D $FAPbI_3$ perovskite cubic structure was formed post-annealing. A zoomed-in view of the PbI_2 peak (Fig. 2b) highlights the relative extent of PbI_2 consumption during the 2D perovskite formation, indicative of the trend: C_6Br > PEAI > OAI. Notably, all 2D percussors were used at identical concentration (2.5 mg mL^{-1}) and under the same spin-coating conditions to ensure comparability of surface coverage. This trend is corroborated by inset optical images in Fig. 2d, which visually demonstrate improved film uniformity and reduced surface roughness in the order of C_6Br > PEAI > OAI > control. A noticeable darkening of the film surface is observed after 2D layer deposition, compared to the brighter control film—consistent with the consumption of surface-residual PbI_2 and formation of a more uniform 2D/3D interface.

Top-view SEM images in Fig. 2d further support this observation. Bright crystal-like features, likely corresponding to unreacted PbI_2, are evident in the control film. These features are significantly diminished in the C_6Br- and PEAI-treated films, which exhibit more compact grain structures with well-closed grain boundaries. OAI-treated films show moderate improvement over the control but still display partially open or incomplete grain boundary closure. These morphological enhancements, along with the apparent reduction in surface-residual PbI_2, are critical for minimizing charge-accumulating defects and suppressing nonradiative recombination by effectively reducing surface trap densities,[44,45] contributing directly to the superior photovoltaic performance observed for C_6Br- and PEAI-passivated devices, as elaborated in the further discussion. The inset optical images show that the passivation layer is uniform.

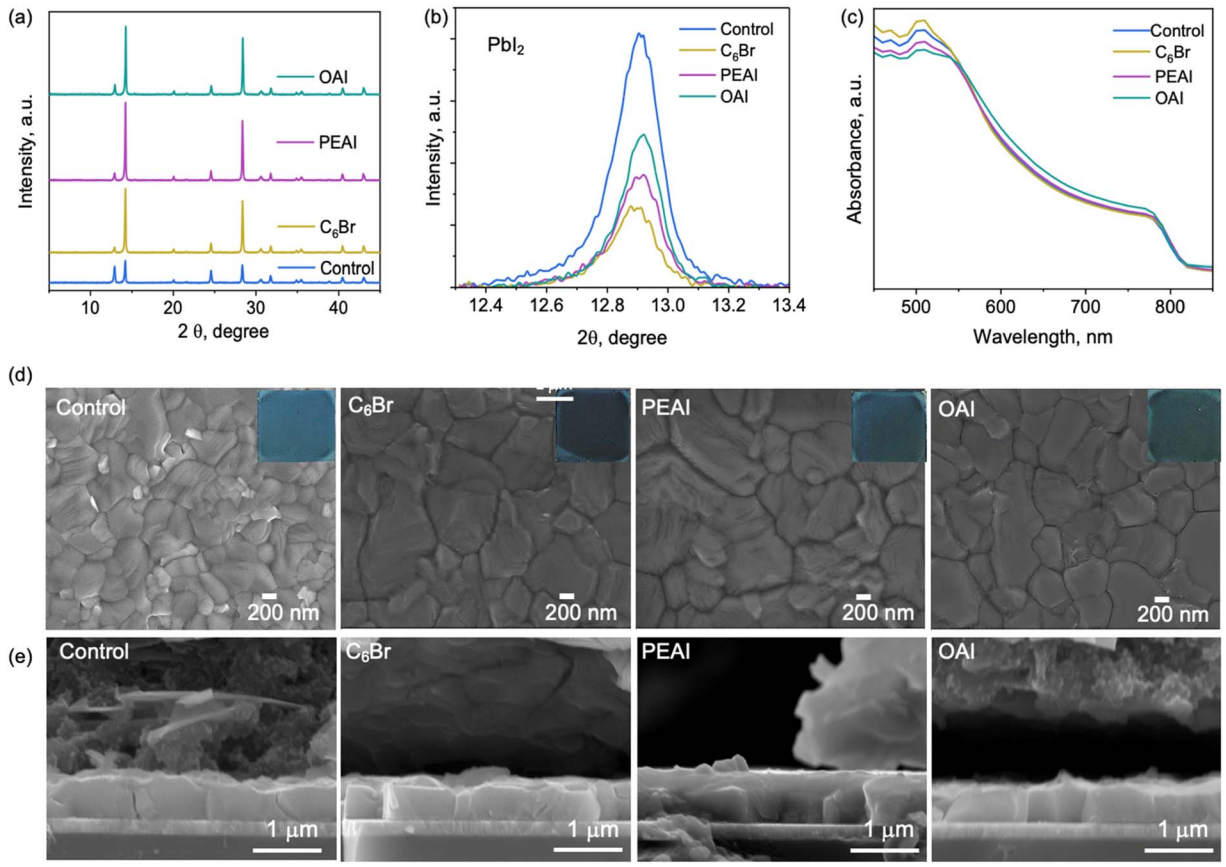

Fig. 2 (a) X-ray diffraction (XRD) patterns comparing perovskite films with different 2D passivation layers. (b) Highlighted PbI_2 peak intensities for each passivation material. (c) UV-Vis absorption spectra of perovskite films with different 2D passivation layers (control, C_6Br, PEAI, and OAI), and (d) scanning electron microscopy (SEM) images illustrating film morphology variations across different 2D passivation treatments. Inset images show the films' corresponding optical picture for the corresponding annealed perovskite film. (e) Cross-sectional SEM images of the perovskite devices with varying layers of passivation.

Cross-sectional SEM images in Fig. 2e show the perovskite films treated with 2D layers and carbon electrodes. While the ultrathin 2D layers are not directly resolved due to contrast limitations, the perovskite films treated with 2D passivation exhibit more compact morphology, with fewer voids or gaps between grains compared to the control. The untreated control film displays visible cracks and intergranular gaps, while the 2D-treated films help to fill grain boundary voids. Additionally, the top surfaces of the C_6Br- and PEAI-treated films are noticeably flatter and more uniform compared to those of the control and OAI-treated samples. To ascertain that the 2D layer did not impact the light absorption of the 3D perovskite, UV-Vis absorption spectroscopy has been carried out, as shown in Fig. 2c. Negligible differences were observed among 2D passivated 3D perovskites. In particular, C_6Br can also improve the light absorption in short wavelengths below 550 nm, suggesting a better device performance by increasing photon to electron conversion.

The effect of 2D passivation layers on photovoltaic performance was measured, as shown in Fig. 3. Fig. 3a presents the current density–voltage (J–V) characteristics for representative devices for the control and C_6Br, PEAI, and OAI passivated perovskites, respectively. C_6Br-passivated devices achieved the highest power conversion efficiency (PCE) of approximately ~21%, followed by PEAI (~19.7%) and OAI (~17.6%), while the control device exhibited a PCE of ~16.57%. The detailed champion device performances are shown in Table 1. The major improvement from employing the 2D passivation is the increase in fill factor from 70.1% of the control to 78.7% of C_6Br, which could be associated with the optimized charge extraction and reduced recombination losses *via* 2D passivation, thereby enhancing the initial photovoltaic performance of carbon-based

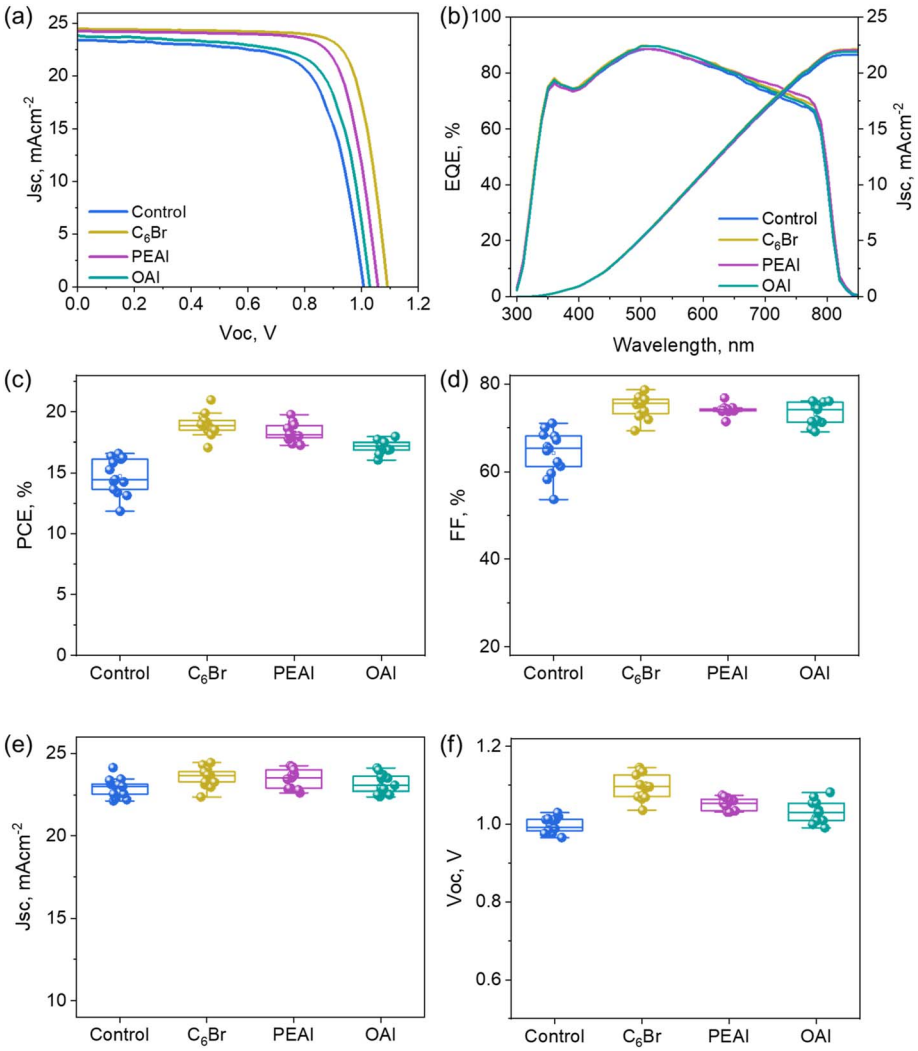

Fig. 3 (a) Current density–voltage (J–V) characteristics under standard illumination conditions, comparing devices with different 2D passivation materials. (b) External quantum efficiency (EQE) spectra for the corresponding devices. Statistical comparison of photovoltaic parameters for perovskite solar cells with different 2D passivation layers (control, C_6Br, PEAI, and OAI), (c) power conversion efficiency (PCE, %), (d) fill factor (FF, %), (e) open-circuit voltage (V_{oc}, V), and (f) short-circuit current density (J_{sc}, mA cm^{-2}). Each data point represents an individual device, with box plots highlighting the distribution, median, and variability within each group.

Table 1 *J–V* parameters for champion devices

2D passivation materials	V_{oc}, V	J_{sc}, mA cm^{-2}	FF, %	PCE, %	$PCE_{average}$, %	Hysteresis index
Control	1.01	23.42	70.1	16.57	14.73 ± 1.48	0.19
C_6Br	1.10	24.47	78.7	20.98	18.95 ± 0.92	0.09
PEAI	1.06	24.25	76.9	19.73	18.31 ± 0.73	0.04
OAI	1.03	23.83	71.8	17.60	17.17 ± 0.52	0.04

perovskite solar cells. In particular, the capability of passivation significantly increases by using C_6Br and PEAI compared with OAI, which is attributed to the increased PbI_2 consumption, as shown in the 2D GIWXAS results.

The external quantum efficiency (EQE) spectra for these 2D passivated perovskite devices have been measured, as show in Fig. 3b, where the 2D layer could improve the conversion in the back surface of the perovskite, yielding improved integrated photocurrents of 22.10 ± 0.1, 22.02 ± 0.1, 21.74 ± 0.1, and 21.61 ± 0.1 mA cm^{-2} for C_6Br, PEAI, OAI, and control devices across the visible spectrum, respectively (Fig. 3b). These values agree with the *J–V* curve derived J_{sc} within ≈2 mA cm^{-2}, confirming experimental consistency. The residual discrepancy likely arises from reflection losses at device interfaces, parasitic absorption in the transport and electrode layers, and spectral mismatch between the solar simulator and the AM 1.5G reference spectrum.[46] In particular, for the carbon-based perovskite solar cell, the interface between the carbon electrode and the perovskite semi-device, *i.e.*, glass/ITO/SnO_2/3D-perovskite/2D-perovskite/spiro-OMeTAD, can also contribute to the photon collection due to the rough surface of the carbon electrode.[47] Statistical comparisons of PCE, open-circuit voltage (V_{oc}), short-circuit current density (J_{sc}), and fill factor (FF) (Fig. 3c–f) further show that C_6Br-treated devices consistently outperform those treated with PEAI, OAI, and the control. In particular, the 2D passivation layer could effectively reduce the series resistivity (R_s) and improve the shunting resistance (R_{sh}), as shown in the ESI Fig. S1,† which are in agreement with the demonstrated passivation effect on surface defects and may also cover pinholes on the 3D perovskite films.

To further elucidate the charge transport mechanisms and underlying device physics for these 2D passivated perovskite devices, we performed steady-state photoluminescence (PL), time-resolved PL (TRPL), capacitance–voltage (*C–V*) profiling, electrochemical impedance spectroscopy (EIS), and light-intensity–dependent measurements (Fig. 4). As shown in the steady-state PL spectra (Fig. 4a), all passivated films exhibit significantly higher emission intensity compared to the unpassivated control, indicating suppressed nonradiative surface recombination due to effective trap and grain boundary passivation on the 3D perovskite surface.[48,49] To further evaluate carrier lifetime, TRPL measurements were performed (Fig. 4b). The extracted carrier lifetimes (τ) follow the order: $\tau_{Control}$ (72.08 ns) < τ_{OAI} (239.68 ns) < τ_{PEAI} (253.70 ns) < τ_{C6Br} (403.74 ns) (ESI Table S1† for carrier lifetime fitting results). Note that the perovskite layer was directly deposited on the glass slides without an electron transport layer to evaluate the carrier transport behavior at the perovskite/passivation interface. The substantial increase in τ for all passivated films confirms the effective suppression of trap-assisted recombination.[50,51] Notably, C_6Br shows the longest lifetime, consistent with its highest PL intensity and superior photovoltaic performance. These results indicate that C_6Br not only reduces nonradiative losses but also promotes longer carrier diffusion lifetimes, key to enhanced charge extraction. Overall, both PL intensity and TRPL lifetime jointly affirm the improved optoelectronic quality imparted by 2D surface passivation for C-PSCs.

To further investigate the recombination process associated with the charge transfer in each of the 2D layer passivated devices, capacitance–voltage (*C–V*) measurements were performed, as shown in Fig. 4c. The governing equation for built-in potential and charge carrier concentration is determined using eqn (1):

$$1/C^2 = 2(V_{bi} - V)/q\varepsilon\varepsilon_0 N \quad (1)$$

where C is the capacitance, V_{bi} is the built-in potential, V is the applied voltage, q is the elementary charge, ε is the relative permittivity, ε_0 is the vacuum permittivity, and N is the charge concentration. The built-in potential deduced from the intercepts of the $1/C^2$–V (Mott–Schottky) plots suggests a notable upward shift for all passivated devices compared to the control. The extracted V_{bi} values are presented as below: C_6Br (1.06 V) > PEAI (1.02 V) > OAI (0.92 V) > control (0.89 V). The improved V_{bi} indicates that 2D layers enhance the internal electric field within the device and promote a better band alignment with the hole transport layer (here, spiro-OMeTAD). Notably, the variation trend of the V_{bi} values closely aligns with the V_{oc} values extracted from the *J–V* curves, as shown in Table 1. The higher the V_{bi}, the greater the driving force for charge separation and collection, which facilitates an increase in V_{oc} and thereby contributes to improved overall device performance. The highest V_{bi} observed for C_6Br suggests enhanced charge separation efficiency, which supports its superior photovoltaic characteristics.[52]

To gain further insights into the charge transport dynamics and recombination processes, electrochemical impedance spectroscopy (EIS) measurements were performed under dark conditions at a forward bias (0.8 V) for all devices. The Nyquist plots exhibit characteristic semicircular arcs for all devices, which were fitted using the equivalent circuit model shown in the inset of Fig. 4d. The model consists of a series resistance (R_s), representing the contact and wiring resistance, in series with a parallel combination of charge transfer resistance (R_{ct}) and a constant phase element (CPE_1), representing interfacial capacitance and non-ideal behavior at the perovskite/carbon

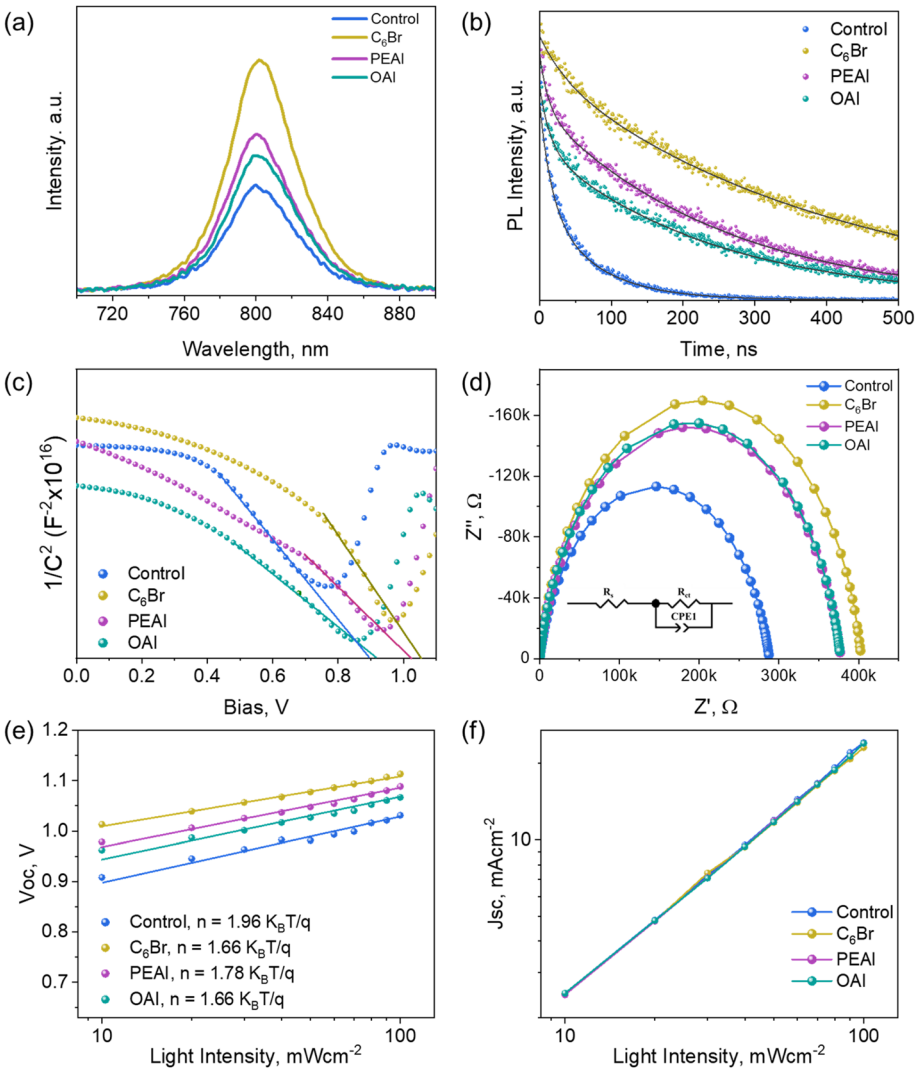

Fig. 4 (a) Steady-state photoluminescence (PL) spectra, (b) time-resolved photoluminescence (TRPL) decay curves, (c) capacitance–voltage (C–V) profiles, (d) electrochemical impedance spectroscopy (EIS) Nyquist plots, (e) dependence of open-circuit voltage (V_{oc}) on illumination intensity, and (f) dependence of short-circuit current density (J_{sc}) on illumination intensity for devices employing various 2D passivation layers.

Table 2 Extracted electrical parameters from impedance spectroscopy for C_6Br-, PEAI-, and OAI-passivated perovskite devices under fresh conditions. The table includes series resistance (R_s), charge transport resistance (R_{ct}), and constant phase element (CPE) values

2D	R_s, Ω	R_{ct}, kΩ	$CPE_1 - T$, F
Control	53.92	287.76	2.37×10^{-8}
C_6Br	65.97	401.93	1.59×10^{-8}
PEAI	31.79	376.28	2.12×10^{-8}
OAI	66.31	376.56	1.70×10^{-8}

interface. The modeled results for the EIS are shown in Table 2. It indicates that the C_6Br, PEAI, and OAI could increase the charge recombination resistance (R_{ct}) and reduce the charge accumulation and trap states at the 2D/3D perovskite interface, which demonstrates the surface passivation using 2D perovskites. In particular, the superior passivation performance of C_6Br may originate from its electronically insulating nature, the stronger interaction with surface defects and effective suppression of halide migration. However, C_6Br also shows a higher series resistance (R_s), which may hinder efficient charge extraction.

To further analyze the recombination mechanisms, light-intensity (I)–dependent J–V curves were measured, as shown in Fig. 4e. The slope of V_{oc} *versus* ln(I) yields ideality factors (n) for the 2D passivated perovskite device, such as 1.96 for the control without passivation, decreasing to 1.66 for both C_6Br and OAI, and 1.78 for PEAI passivated perovskite devices. Values of $n > 1$ typically indicate the presence of trap-assisted recombination. These extracted ideality factors indicate a notable suppression of trap-assisted (Shockley–Read–Hall) recombination in all passivated devices, particularly in those treated with C_6Br and OAI. Notably, both C_6Br and OAI show similar ideality factors ($n \approx 1.66$), suggesting comparable suppression of trap-mediated recombination. Despite this,

the C_6Br-treated device exhibits lower PCE than the OAI-treated device, which implies that factors beyond recombination—such as interfacial charge transport or energetic alignment—may be limiting its performance. The photocurrent behavior under variable light intensity was also investigated by plotting the short-circuit current density (J_{sc}) as a function of illumination (Fig. 4f). All devices show a linear relationship on the log–log scale, indicating minimal bimolecular recombination. The power-law fitting ($J_{sc} \propto I^{\alpha}$) yields α values close to unity for all samples, confirming efficient photocarrier generation and collection. While the curves in Fig. 4f visually overlap, the precise α values differ slightly ($\alpha =$ 0.98 for OAI, 0.95 for C_6Br), reflecting subtle distinctions in carrier recombination under short-circuit conditions. The slightly lower α in C_6Br-treated devices suggests a marginally higher degree of recombination loss at a short circuit, potentially due to incomplete passivation or increased carrier extraction barriers. Taken together, these results indicate that while C_6Br effectively suppresses trap-assisted recombination (as evidenced by EIS and V_{oc} measurements), its increased series resistance and slightly less ideal α value under short-circuit conditions may contribute to its relatively lower device efficiency compared to OAI.

The long-term operational stability of unencapsulated carbon-based PSCs was evaluated under continuous 1 sun illumination and both inert and ambient air conditions, with surface wettability characterized by water contact angle measurements, as shown in Fig. 5. Note that all devices were unencapsulated. Fig. 5a shows the stabilized power output (SPO) corresponding to the maximum power point of each device. All passivated devices retain over 98% of their initial output over 200 seconds, whereas the control device declines to around 88%. Fig. 5b shows the stability for this device measured *via* maximum power point tracking (MPPT) for 300 minutes. It is observed that C_6Br, OAI, and PEAI-treated devices exhibit slower degradation. In particular, C_6Br and OAI passivation improve initial photovoltaic metrics and stabilize device output under continuous operational stress. Furthermore, long-term stability was further probed by storing devices at open-circuit under an inert N_2 atmosphere for 500 h, as shown in Fig. 5c. C_6Br and OAI-passivated devices retain nearly their initial PCE, while PEAI and control devices decline to ~65% and ~50%, respectively. In dry air (Fig. 5d), OAI-treated devices exhibit the greatest resilience, retaining ~80% of their starting efficiency; C_6Br devices retain ~60%, PEAI ~50%, and the control falls below 20%. These results underscore OAI's superior moisture resistance and C_6Br's robust inert-environmental performance. The exceptional stability of our 2D-passivated devices aligns with previous reports showing that appropriate interfacial engineering in carbon-based PSCs can yield remarkable ambient storage stability, with some systems retaining nearly 90% of efficiency

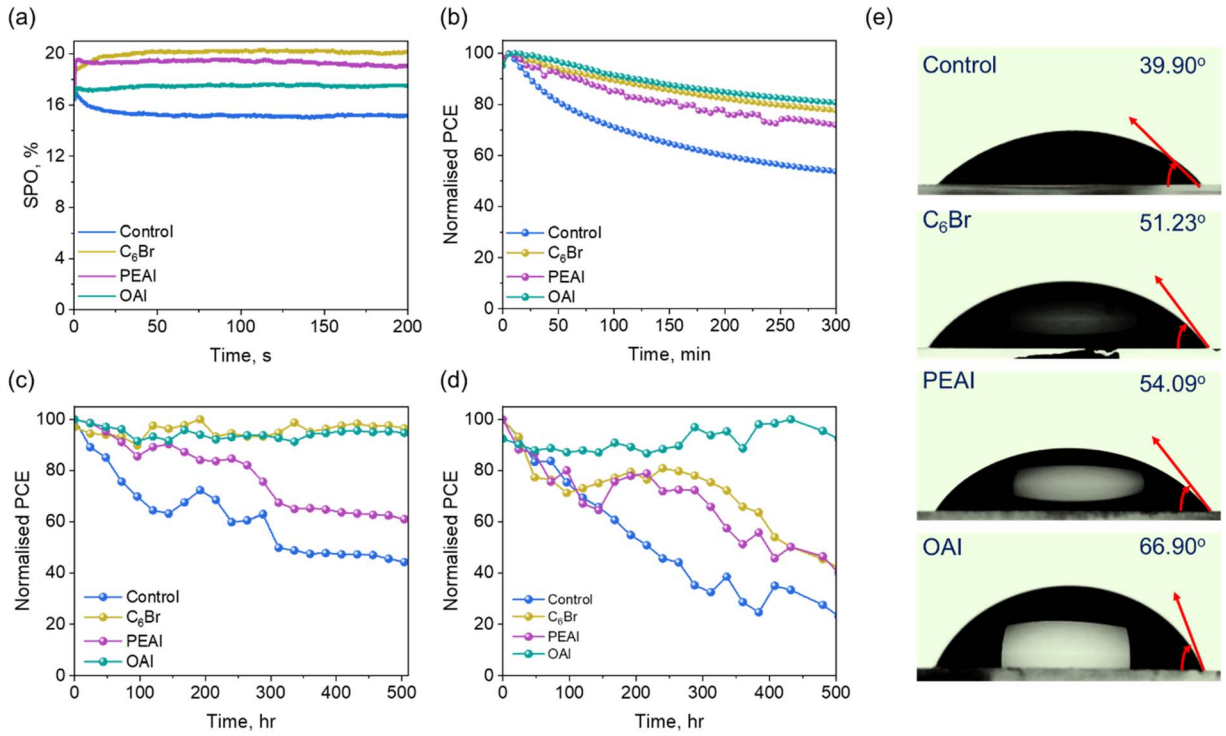

Fig. 5 (a) Stabilized power output (SPO) measured for 200 s at a fixed voltage near the maximum power point (MPP) derived from *J*–*V* curves. (b) Maximum power point tracking (MPPT) performance for unencapsulated perovskite solar cells under continuous illumination (100 mW cm^{-2}) for 300 minutes. (c) Long-term operational stability of unencapsulated perovskite devices under an inert nitrogen atmosphere, comparing different 2D passivation layers. (d) Long-term operational stability of unencapsulated perovskite devices exposed to ambient air with low humidity (<5% RH), comparing different 2D passivation layers. (e) Water contact angle measurements of perovskite films with different 2D passivation layers.

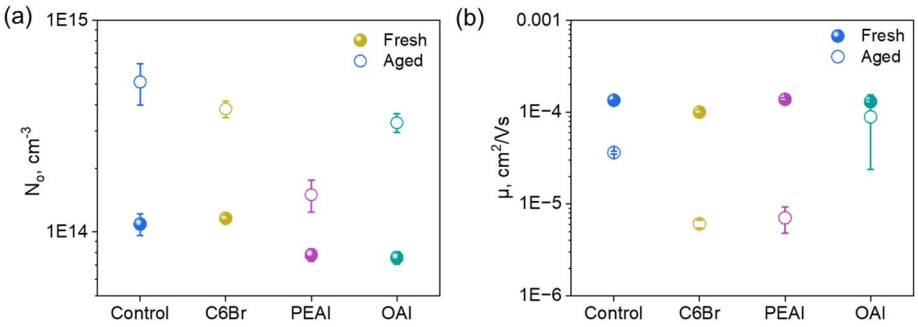

Fig. 6 (a) Mobile ion concentration (N_0), and (b) ionic mobility (μ) measured in fresh and aged perovskite solar cell devices with different 2D passivation layers: control, C_6Br, PEAI, and OAI. Fresh devices are represented by solid dots and aged devices by circles.

after thousands of hours.[53] As shown in Fig. 5e, water contact angle measurements have been employed to check the extent to which these films repel water: control films exhibit a contact angle of 39.9°, whereas C_6Br, PEAI, and OAI yield progressively higher angles of 51.2°, 54.1°, and 66.9°, respectively. The increased hydrophobicity imparted by OAI and C_6Br correlates directly with enhanced ambient stability.

To investigate the influence of 2D passivation on the ion migration-related stability behavior, we first investigated the mobile ion concentration (N_0) and ionic mobility (μ) in fresh devices. These devices were then stored in a nitrogen-filled glovebox for 10 days (aged devices) and remeasured. The results are presented in Fig. 6a and b, with further details provided in the ESI, Table S2.† The detailed methodology used for these measurements is provided in the ESI, Note 1.[54,55] Fresh control devices without 2D passivation exhibit the highest mobile ion concentration, $N_0 \sim 1.09 \times 10^{14}$ cm^{-3}, reflecting a significant number of ionic defects. After aging, the mobile ion concentration significantly increased to 5.12×10^{14} cm^{-3}. In contrast, 2D perovskite-passivated devices show markedly lower mobile ion concentration both in fresh and aged devices, further indicating the effective passivation of ion migration pathways *via* a 2D layer. Although ion concentration increases across all samples after aging, the 2D passivated devices maintain lower ion concentration values than in the control, predicting improved long-term stability. As for the ionic mobility (μ), the control without 2D passivation shows an ionic mobility drop from 1.35×10^{-4} to 3.63×10^{-6} cm^2 V^{-1} s^{-1} after aging, while C_6Br-treated films retain the lowest mobility ($1.00 \times 10^{-4} \rightarrow 6.07 \times 10^{-7}$ cm^2 V^{-1} s^{-1}), followed by PEAI ($1.39 \times 10^{-4} \rightarrow 7.05 \times 10^{-6}$ cm^2 V^{-1} s^{-1}). Interestingly, OAI exhibits the highest aged-state mobility (8.93×10^{-5} cm^2 V^{-1} s^{-1}), consistent with its less effective ionic blocking behavior. These results demonstrate that 2D passivation can lower ion mobility, particularly with C_6Br and PEAI, effectively reducing both the concentration and transport of mobile ions. These 2D layers may act as ion diffusion barriers and can reduce ion trapping or reduce transport channels to effectively increase stability. In particular, the degree of suppression varies: C_6Br and PEAI are more effective than OAI.

Overall, 2D passivation not only elevates initial device performance but also imparts significant environmental resilience. OAI-passivated C-PSCs demonstrate the most robust stability under ambient conditions, while C_6Br-passivated devices offer near-ideal durability in inert atmospheres. These stability improvements can be mechanistically connected to our earlier ionic transport measurements (Fig. 6a and b), where we observed that passivation layers—particularly OAI and C_6Br—significantly reduced mobile ion concentration and mobility in aged devices[39,56] By creating effective barriers against both moisture ingress and ion migration, 2D passivation layers address two critical degradation pathways in carbon-based perovskite solar cells.

Conclusion

In summary, we have demonstrated that 2D passivation on the carbon-based perovskite device could not only improve power conversion efficiency but also effectively improve stability. In particular, our study systematically compared *n*-hexylammonium bromide (C_6Br), phenethylammonium iodide (PEAI), and *n*-octylammonium iodide (OAI) as passivation agents for carbon-based perovskite solar cells fully processed in an air ambient atmosphere. C_6Br-treated devices achieved a PCE of ~21% due to superior defect passivation, suppressed recombination, and enhanced charge extraction, while OAI-passivated cells exhibited the best ambient stability, retaining over 80% of their initial performance after 500 hours in air. Both C_6Br and OAI significantly reduced mobile ion concentration and mobility, correlating with improved operational stability. This work provides actionable guidelines for the molecular engineering of 2D/3D perovskite interfaces, paving the way toward robust, scalable, and commercially viable carbon-based perovskite solar technologies.

Data availability

The data supporting this article have been included as part of the ESI.† The other data are available on request to the corresponding authors.

Conflicts of interest

The authors declare no conflict of interest.

Acknowledgements

This work was supported by the Department of Energy, Energy Efficiency and Renewable Energy under award DE-EE0009833. This work was also supported by the National Science Foundation under contract no. ECCS-2413632, MOMS-2330728, TI-2329871, DMR-2330738, CMMI-2226918, DMREF-2323766, and ECCS-2339233.

References

1 *Best Research-Cell Efficiency Chart*, **https://www.nrel.gov/pv/cell-efficiency.html**, 2025.
2 N. J. Jeon, J. H. Noh, W. S. Yang, Y. C. Kim, S. Ryu, J. Seo and S. I. Seok, Compositional engineering of perovskite materials for high-performance solar cells, *Nature*, 2015, **517**, 476–480.
3 Y. Li, L. Ji, R. Liu, C. Zhang, C. H. Mak, X. Zou, H.-H. Shen, S.-Y. Leu and H.-Y. Hsu, A review on morphology engineering for highly efficient and stable hybrid perovskite solar cells, *J. Mater. Chem. A*, 2018, **6**, 12842–12875.
4 S. Teale, M. Degani, B. Chen, E. H. Sargent and G. Grancini, Molecular cation and low-dimensional perovskite surface passivation in perovskite solar cells, *Nat. Energy*, 2024, **9**, 779–792.
5 A. Ali, Y. Ahn, K. A. Khawaja, J. H. Kang, Y. J. Park, J. H. Seo and B. Walker, A Simple Cu(II) Polyelectrolyte as a Method to Increase the Work Function of Electrodes and Form Effective p-Type Contacts in Perovskite Solar Cells, *Adv. Funct. Mater.*, 2021, **31**, 2009246.
6 N. Ahn and M. Choi, Towards Long-Term Stable Perovskite Solar Cells: Degradation Mechanisms and Stabilization Techniques, *Adv. Sci.*, 2024, **11**, 2306110.
7 C. Zhao, Z. Zhou, M. Almalki, M. A. Hope, J. Zhao, T. Gallet, A. Krishna, A. Mishra, F. T. Eickemeyer, J. Xu, Y. Yang, S. M. Zakeeruddin, A. Redinger, T. J. Savenije, L. Emsley, J. Yao, H. Zhang and M. Grätzel, Stabilization of highly efficient perovskite solar cells with a tailored supramolecular interface, *Nat. Commun.*, 2024, **15**, 7139.
8 C. Yang, W. Hu, J. Liu, C. Han, Q. Gao, A. Mei, Y. Zhou, F. Guo and H. Han, Achievements, challenges, and future prospects for industrialization of perovskite solar cells, *Light Sci. Appl.*, 2024, **13**, 227.
9 J. He, Y. Bai, Z. Luo, R. Ran, W. Zhou, W. Wang and Z. Shao, Advanced carbon-based rear electrodes for low-cost and efficient perovskite solar cells, *Energy Environ. Sci.*, 2025, **18**, 2136–2164.
10 M. Stefanelli, L. Vesce and A. Di Carlo, Upscaling of Carbon-Based Perovskite Solar Module, *Nanomaterials*, 2023, **13**, 313.
11 M. Que, B. Zhang, J. Chen, X. Yin and S. Yun, Carbon-based electrodes for perovskite solar cells, *Mater. Adv.*, 2021, **2**, 5560–5579.
12 S. Zouhair, C. Clegg, I. Valitova, S. March, J. M. Jailani and V. Pecunia, Carbon Electrodes for Perovskite Photovoltaics: Interfacial Properties, Meta-analysis, and Prospects, *Sol. RRL*, 2024, **8**, 2300929.
13 F. Pei, Y. Chen, Q. Wang, L. Li, Y. Ma, H. Liu, Y. Duan, T. Song, H. Xie, G. Liu, N. Yang, Y. Zhang, W. Zhou, J. Kang, X. Niu, K. Li, F. Wang, M. Xiao, G. Yuan, Y. Wu, C. Zhu, X. Wang, H. Zhou, Y. Wu and Q. Chen, A binary 2D perovskite passivation for efficient and stable perovskite/silicon tandem solar cells, *Nat. Commun.*, 2024, **15**, 7024.
14 D. B. Khadka, Y. Shirai, M. Yanagida, H. Ota, A. Lyalin, T. Taketsugu and K. Miyano, Defect passivation in methylammonium/bromine free inverted perovskite solar cells using charge-modulated molecular bonding, *Nat. Commun.*, 2024, **15**, 882.
15 F. Zhang, B. Tu, S. Yang, K. Fan, Z. Liu, Z. Xiong, J. Zhang, W. Li, H. Huang, C. Yu, A. K.-Y. Jen and K. Yao, Buried-Interface Engineering of Conformal 2D/3D Perovskite Heterojunction for Efficient Perovskite/Silicon Tandem Solar Cells on Industrially Textured Silicon, *Adv. Mater.*, 2023, **35**, 2303139.
16 J. Wen, Y. Zhao, P. Wu, Y. Liu, X. Zheng, R. Lin, S. Wan, K. Li, H. Luo, Y. Tian, L. Li and H. Tan, Heterojunction formed via 3D-to-2D perovskite conversion for photostable wide-bandgap perovskite solar cells, *Nat. Commun.*, 2023, **14**, 7118.
17 K. M. Yeom, C. Cho, E. H. Jung, G. Kim, C. S. Moon, S. Y. Park, S. H. Kim, M. Y. Woo, M. N. T. Khayyat, W. Lee, N. J. Jeon, M. Anaya, S. D. Stranks, R. H. Friend, N. C. Greenham and J. H. Noh, Quantum barriers engineering toward radiative and stable perovskite photovoltaic devices, *Nat. Commun.*, 2024, **15**, 4547.
18 W. Ke, L. Mao, C. C. Stoumpos, J. Hoffman, I. Spanopoulos, A. D. Mohite and M. G. Kanatzidis, Compositional and Solvent Engineering in Dion–Jacobson 2D Perovskites Boosts Solar Cell Efficiency and Stability, *Adv. Energy Mater.*, 2019, **9**, 1803384.
19 F. U. Kosasih and C. Ducati, Attaining High Photovoltaic Efficiency and Stability with Multidimensional Perovskites, *ChemSusChem*, 2018, **11**, 4193–4202.
20 L. N. Quan, M. Yuan, R. Comin, O. Voznyy, E. M. Beauregard, S. Hoogland, A. Buin, A. R. Kirmani, K. Zhao, A. Amassian, D. H. Kim and E. H. Sargent, Ligand-Stabilized Reduced-Dimensionality Perovskites, *J. Am. Chem. Soc.*, 2016, **138**, 2649–2655.
21 I. Spanopoulos, I. Hadar, W. Ke, Q. Tu, M. Chen, H. Tsai, Y. He, G. Shekhawat, V. P. Dravid, M. R. Wasielewski, A. D. Mohite, C. C. Stoumpos and M. G. Kanatzidis, Uniaxial Expansion of the 2D Ruddlesden–Popper Perovskite Family for Improved Environmental Stability, *J. Am. Chem. Soc.*, 2019, **141**, 5518–5534.
22 J. Zhang, X. Peng, H. Wu, G. Zhang, Y. Chen, W. Cai, Z. Pan, H. Rao and X. Zhong, Comprehensive Passivation of Surface and Bulk Defects in Perovskite for High Efficiency Carbon-Based CsPbI3 Solar Cells, *Angew. Chem., Int. Ed.*, 2025, **64**, e202423655.
23 J. Tang, Y. Lin, H. Yan, J. Lin, H. Rao, Z. Pan and X. Zhong, 20.1 % Certified Efficiency of Planar Hole Transport Layer-Free Carbon-Based Perovskite Solar Cells by Spacer Cation

Chain Length Engineering of 2D Perovskites, *Angew. Chem., Int. Ed.*, 2024, **63**, e202406167.

24 S. Zouhair, S.-M. Yoo, D. Bogachuk, J. P. Herterich, J. Lim, H. Kanda, B. Son, H. J. Yun, U. Würfel, A. Chahboun, M. K. Nazeeruddin, A. Hinsch, L. Wagner and H. Kim, Employing 2D-Perovskite as an Electron Blocking Layer in Highly Efficient (18.5%) Perovskite Solar Cells with Printable Low Temperature Carbon Electrode, *Adv. Energy Mater.*, 2022, **12**, 2200837.

25 S. Dai, H. Cao, W. Sharmoukh, Y. Qiang, L. Zhao, Y. Chen, Y. Li, H. N. Abdelhamid, N. Taghavinia and Z. Yu, Pure-phase two-dimensional perovskite capping layer enables high-performance and durable carbon-based photovoltaics, *Chem. Eng. J.*, 2024, **497**, 154611.

26 P. Saivineeth, T. Favian, L. Muzhi, K. K. Ali, Y. Feng and R. Nicholas, Use of carbon electrodes to reduce mobile ion concentration and improve reliability of metal halide perovskite photovoltaics, *Energy Mater.*, 2024, **4**, 400060.

27 X.-Z. Zhu, K.-L. Wang, J.-G. Wang, Y.-H. Hao, J.-H. Chen, N. Nizamani, Y. Liu, Z.-K. Wang and L.-S. Liao, 2D Perovskite Capping Layer Enabling Stable Perovskite Photovoltaics, *Sol. RRL*, 2024, **8**, 2301082.

28 M. Li, J. Zhou, L. Tan, Y. Liu, S. Wang, C. Jiang, H. Li, X. Zhao, X. Gao, W. Tress, L. Ding and C. Yi, Brominated PEAI as Multi-Functional Passivator for High-Efficiency Perovskite Solar Cell, *Energy Environ. Mater.*, 2023, **6**, e12360.

29 S. M. Park, M. Wei, J. Xu, H. R. Atapattu, F. T. Eickemeyer, K. Darabi, L. Grater, Y. Yang, C. Liu, S. Teale, B. Chen, H. Chen, T. Wang, L. Zeng, A. Maxwell, Z. Wang, K. R. Rao, Z. Cai, S. M. Zakeeruddin, J. T. Pham, C. M. Risko, A. Amassian, M. G. Kanatzidis, K. R. Graham, M. Grätzel and E. H. Sargent, Engineering ligand reactivity enables high-temperature operation of stable perovskite solar cells, *Science*, 2023, **381**, 209–215.

30 G. Lucarelli, F. De Rossi, B. Taheri, T. M. Brown and F. Brunetti, Phenethylammonium Iodide Passivation Layers for Flexible Planar Perovskite Solar Cells, *Energy Technol.*, 2022, **10**, 2200314.

31 Y. Bai, S. Xiao, C. Hu, T. Zhang, X. Meng, H. Lin, Y. Yang and S. Yang, Dimensional Engineering of a Graded 3D–2D Halide Perovskite Interface Enables Ultrahigh Voc Enhanced Stability in the p-i-n Photovoltaics, *Adv. Energy Mater.*, 2017, **7**, 1701038.

32 Q. Jiang, Y. Zhao, X. Zhang, X. Yang, Y. Chen, Z. Chu, Q. Ye, X. Li, Z. Yin and J. You, Surface passivation of perovskite film for efficient solar cells, *Nat. Photonics*, 2019, **13**, 460–466.

33 S. You, F. T. Eickemeyer, J. Gao, J.-H. Yum, X. Zheng, D. Ren, M. Xia, R. Guo, Y. Rong, S. M. Zakeeruddin, K. Sivula, J. Tang, Z. Shen, X. Li and M. Grätzel, Bifunctional hole-shuttle molecule for improved interfacial energy level alignment and defect passivation in perovskite solar cells, *Nat. Energy*, 2023, **8**, 515–525.

34 Y. Feng, R. Liu, F. Li, M. Jin, Q. Du, Y. Rong, H. Hu, M. Wang, Y. Li, Z. Shen, Y. Liu, H. Li and C. Chen, A synergistic co-passivation strategy for high-performance perovskite solar cells with large open circuit voltage, *J. Mater. Chem. C*, 2022, **10**, 12699–12707.

35 R. Chen, L. Gu, J. Su, Y. Feng, H. Deng, J. Zhang, Y. Bao, D. Wang, X. Song, L. Zhao and L. Song, Stabilizing 2D perovskite passivation layer with mixed spacer cations for efficient and stable perovskite solar cells, *Nano Energy*, 2025, **139**, 110904.

36 D. Li, Z. Xing, X. Meng, X. Hu, T. Hu and Y. Chen, Selection of Functional Spacer Cations for Efficient 2D/3D Perovskite Solar Cells, *CCS Chem.*, 2023, **5**, 781–801.

37 S. Mondal, N. Eguchi, N. Nishimura, Y. Hinuma, K. Yamamoto, A. Kogo, T. N. Murakami and H. Kanda, Mixed 2D-cation passivation towards improved durability of perovskite solar cells and dynamics of 2D-perovskites under light irradiation and at high temperature, *Sustain. Energy Fuels*, 2025, **9**, 247–255.

38 N. Nishimura, H. Kanda, R. Katoh, A. Kogo and T. N. Murakami, Thermally stable phenylethylammonium-based perovskite passivation: spontaneous passivation with phenylethylammonium bis(trifluoromethylsulfonyl) imide during deposition of PTAA for enhancing photovoltaic performance of perovskite solar cells, *J. Mater. Chem. A*, 2024, **12**, 15631–15640.

39 Z. G. Karabag, A. Karabag, U. Gunes, X.-X. Gao, O. A. Syzgantseva, M. A. Syzgantseva, F. V. Yaylali, N. Shibayama, H. Kanda, A. I. Rafieh, R. C. Turnell-Ritson, P. J. Dyson, S. Yerci, M. K. Nazeeruddin and G. Gunbas, Tuning 2D Perovskite Passivation: Impact of Electronic and Steric Effects on the Performance of 3D/2D Perovskite Solar Cells, *Adv. Energy Mater.*, 2023, **13**, 2302038.

40 H. Zhang, J. Xiao, J. Shi, H. Su, Y. Luo, D. Li, H. Wu, Y.-B. Cheng and Q. Meng, Self-Adhesive Macroporous Carbon Electrodes for Efficient and Stable Perovskite Solar Cells, *Adv. Funct. Mater.*, 2018, **28**, 1802985.

41 A. H. Proppe, A. Johnston, S. Teale, A. Mahata, R. Quintero-Bermudez, E. H. Jung, L. Grater, T. Cui, T. Filleter, C.-Y. Kim, S. O. Kelley, F. De Angelis and E. H. Sargent, Multication perovskite 2D/3D interfaces form via progressive dimensional reduction, *Nat. Commun.*, 2021, **12**, 3472.

42 Y. Boeije, W. T. M. Van Gompel, Y. Zhang, P. Ghosh, S. J. Zelewski, A. Maufort, B. Roose, Z. Y. Ooi, R. Chowdhury, I. Devroey, S. Lenaers, A. Tew, L. Dai, K. Dey, H. Salway, R. H. Friend, H. Sirringhaus, L. Lutsen, D. Vanderzande, A. Rao and S. D. Stranks, Tailoring Interlayer Charge Transfer Dynamics in 2D Perovskites with Electroactive Spacer Molecules, *J. Am. Chem. Soc.*, 2023, **145**, 21330–21343.

43 S. Wang, S. Kalyanasundaram, L. Gao, Z. Ling, Z. Zhou, M. Bonn, P. W. M. Blom, H. I. Wang, W. Pisula and T. Marszalek, Unveiling the role of linear alkyl organic cations in 2D layered tin halide perovskite field-effect transistors, *Mater. Horiz.*, 2024, **11**, 1177–1187.

44 Y. Chen, Q. Meng, Y. Xiao, X. Zhang, J. Sun, C. B. Han, H. Gao, Y. Zhang, Y. Lu and H. Yan, Mechanism of PbI2 in Situ Passivated Perovskite Films for Enhancing the Performance of Perovskite Solar Cells, *ACS Appl. Mater. Interfaces*, 2019, **11**, 44101–44108.

45 B. Roose, K. Dey, Y.-H. Chiang, R. H. Friend and S. D. Stranks, Critical Assessment of the Use of Excess

Lead Iodide in Lead Halide Perovskite Solar Cells, *J. Phys. Chem. Lett.*, 2020, **11**, 6505–6512.
46 M. Saliba and L. Etgar, Current Density Mismatch in Perovskite Solar Cells, *ACS Energy Lett.*, 2020, **5**, 2886–2888.
47 K. A. Khawaja, W. Xiang, J. Wall, X. Gu, L. Li and F. Yan, Hole transport layer selection for stable and efficient carbon electrode-based perovskite solar cells, *RSC Adv.*, 2025, **15**, 13681–13690.
48 S. Cacovich, G. Vidon, M. Degani, M. Legrand, L. Gouda, J.-B. Puel, Y. Vaynzof, J.-F. Guillemoles, D. Ory and G. Grancini, Imaging and quantifying non-radiative losses at 23% efficient inverted perovskite solar cells interfaces, *Nat. Commun.*, 2022, **13**, 2868.
49 X. Huangfu, J. Chen, G. Ge, J. Li, J. Zhang, Q. Lin, H. Xu and S. M. Wang, 2D/3D Perovskite Surface Passivation-Enabled High-Detectivity Near-Infrared Photodiodes, *Sensors*, 2025, **25**, 2740.
50 Y. Yuan, G. Yan, C. Dreessen, T. Rudolph, M. Hülsbeck, B. Klingebiel, J. Ye, U. Rau and T. Kirchartz, Shallow defects and variable photoluminescence decay times up to 280 μs in triple-cation perovskites, *Nat. Mater.*, 2024, **23**, 391–397.
51 J. Y. Ye, J. Tong, J. Hu, C. Xiao, H. Lu, S. P. Dunfield, D. H. Kim, X. Chen, B. W. Larson, J. Hao, K. Wang, Q. Zhao, Z. Chen, H. Hu, W. You, J. J. Berry, F. Zhang and K. Zhu, Enhancing Charge Transport of 2D Perovskite Passivation Agent for Wide-Bandgap Perovskite Solar Cells Beyond 21%, *Sol. RRL*, 2020, **4**, 2000082.
52 W. Qi, J. Li, Y. Li, K. Sohail, H. Ling, P. Wang, S. Jiao, F. Liu, X. Zhou, H. Wang, D. Zhang, Y. Ding, X. Chen, G. Hou, J. Luo, Y. Zhao, Y. Li and X. Zhang, Manipulated Crystallization and Passivated Defects for Efficient Perovskite Solar Cells via Addition of Ammonium Iodide, *ACS Appl. Mater. Interfaces*, 2021, **13**, 34053–34063.
53 M. Brown and D. Li, Interfacial engineering for high performance carbon-based perovskite solar cells, *Front. Energy Res.*, 2024, **12**, 1.
54 S. Penukula, R. E. Torrejon and N. Rolston, Quantifying and Reducing Ion Migration in Metal Halide Perovskites through Control of Mobile Ions, *Molecules*, 2023, **28**, 5026.
55 S. Penukula, M. N. Khanal, M. Sharma, M. Parashar, R. A. Kerner, M. Chen, M. A. Davis, R. A. Saha, E. Solano, M. B. J. Roeffaers, J. J. Berry, J. M. Luther, J. A. Steele, A. Palmstrom, V. R. Whiteside, B. Rout, I. R. Sellers and N. Rolston, Barrier layer design reduces top electrode ion migration in perovskite solar cells, *EES Solar*, 2025, **1**, 345.
56 T. L. Leung, I. Ahmad, A. A. Syed, A. M. C. Ng, J. Popović and A. B. Djurišić, Stability of 2D and quasi-2D perovskite materials and devices, *Commun. Mater.*, 2022, **3**, 63.